FEDReD. II. 3D extinction map with 2MASS and Gaia DR2 data

Clément Hottier, Carine Babusiaux, Frédéric Arenou

A&A 641, A79 (2020)
https://doi.org/10.1051/0004-6361/202037573

Astronomy & Astrophysics

FEDReD

II. 3D extinction map with 2MASS and *Gaia* DR2 data⋆

C. Hottier[1], C. Babusiaux[2,1], and F. Arenou[1]

[1] GEPI, Observatoire de Paris, PSL University, CNRS, 5 Place Jules Janssen 92190 Meudon, France
e-mail: clement.hottier@obspm.fr
[2] Univ. Grenoble Alpes, CNRS, IPAG, 38000 Grenoble, France

Received 24 January 2020 / Accepted 18 June 2020

ABSTRACT

Aims. We aim to map the 3D distribution of the interstellar extinction of the Milky Way disc up to distances larger than those probed with the *Gaia* parallax alone.
Methods. We applied the FEDReD (Field Extinction-Distance Relation Deconvolver) algorithm to the 2MASS near-infrared photometry together with the *Gaia* DR2 astrometry and photometry. This algorithm uses a Bayesian deconvolution approach, based on an empirical HR-diagram representative of the local thin disc, in order to map the extinction as a function of distance of various fields of view.
Results. We analysed more than 5.6 million stars to obtain an extinction map of the entire Galactic disc within $|b| < 0.24°$. This map provides information up to 5 kpc in the direction of the Galactic centre and more than 7 kpc in the direction of the anticentre. This map reveals the complete shape of structures that are known locally, such as the Vela complex and the split of the local arm. Furthermore, our extinction map shows many large "clean bubbles", especially the one in the Sagittarius-Carina complex, and four others, which define a structure that we nickname the butterfly.

Key words. dust, extinction – ISM: structure

1. Introduction

The interstellar extinction attenuates the light coming from background objects. Moreover this attenuation is a function of the wavelength of radiation, which causes the reddening phenomenon. The study of extinction is necessary to recovering the absolute magnitude and intrinsic colours of Galactic or extragalactic stars.

Mapping the extinction also provides access to the distribution of dust. This component of the Galactic disc is itself an interesting key to understanding the evolution of the Milky Way. In fact, high dust-density areas are expected to be associated with high star-formation regions. Mapping the extinction of the Galactic disc is thus a way to study the spatial structure of spiral arms.

Over the past few decades, several methods of drawing 3D extinction maps of the Galactic disc have been developed. The first results were obtained, with limited resolution and distances, by Fitzgerald (1968), Neckel & Klare (1980), Arenou et al. (1992) and Hakkila et al. (1997). Marshall et al. (2006) compared the Two Micron All Sky Survey(2MASS) photometry to the stellar population synthesis of the Besançon Model (Robin et al. 2012) to obtain extinction density. This approach was also used by Chen et al. (2013) and Schultheis et al. (2014), who added the Glimpse and VVV catalogue to their dataset. Sale et al. (2014) applied a hierarchical Bayesian method to infer stellar properties and extinction profiles with the IPHAS survey. Green et al. (2014), also using a Bayesian method, derived an extinction map from Pan-STARRS data, later combined with 2MASS data (Green et al. 2015, 2018) and the second *Gaia* data release (*Gaia* DR2; Green et al. 2019) data. Capitanio et al. (2017) and Lallement et al. (2019) used a Bayesian inversion technique described in Vergely et al. (2001) on composite dust proxies with *Gaia* DR1 parallax and on 2MASS crosmatched with *Gaia* DR2 respectively. Rezaei Kh. et al. (2018) developed a non-parametric 3D inversion on APOGEE data to obtain a density map of the solar neighbourhood. Chen et al. (2019a) used a random forest algorithm on the crossmatch of *Gaia* DR2, 2MASS and WISE, trained on spectroscopic data, to infer the local extinction density.

In this work, we use the Field Extinction-Distance Relation Deconvolver (FEDReD) algorithm described in Babusiaux et al. (2020). This is a Bayesian deconvolution algorithm that uses an empirical HR diagram to study photometry and parallax in order to derive the extinction as a function of distance as well as the stellar distance distribution, taking into account the completeness of the field of view under study. We applied the algorithm to data from the 2MASS (Skrutskie et al. 2006) crossmatched with the *Gaia* DR2 (Gaia Collaboration 2018). This paper is organised as follows: in Sect. 2 we present the data and filters that we used to select stars. Section 3 is a quick summary of the FEDReD method. In Sect. 4 we describe our method for merging every field of view result into a self-consistent map. Section 5 presents our extinction map, with the details of the different visible features and their relation to the other components of the Galactic disc.

2. Data

This work uses photometry and astrometry based on two surveys, *Gaia* and 2MASS. *Gaia* DR2 data provides high precision parallax and photometry in the G, G_{BP}, and G_{RP} bands; 2MASS

⋆ Full Tables 1–5 and the extinction map are only available at the CDS via anonymous ftp to cdsarc.u-strasbg.fr (130.79.128.5) or via http://cdsarc.u-strasbg.fr/viz-bin/cat/J/A+A/641/A79

provides photometry in three near-infrared bands: J, H, and K_s. Since *Gaia* DR2 and 2MASS are full sky surveys, we were able to draw an extinction map of the entire Galactic disc.

The 2MASS catalogue is used as a basis for our analysis, as its completeness is easier to model than the *Gaia* DR2 completeness, the latter being more dependent on the crowding as well as on the *Gaia*'s scanning law. Every star that we study, therefore, has 2MASS photometry which can be completed that *Gaia*-DR2 parallax, photometry, or both.

To select stars in the 2MASS catalogue, we used the `ph_qual` flag and kept every star with at least a `ph_qual = D` for each photometric band. We used the *Gaia*-2MASS crossmatch provided by Marrese et al. (2019). When a 2MASS source had more than one *Gaia* best neighbour, we did not associate any *Gaia* information with the 2MASS source.

For the *Gaia* photometry (Evans et al. 2018), we did not use G_{BP} or G_{RP} photometry for stars affected by crowding issues using the filter `phot_bp_rp_excess_factor` $> 1.3 + 0.06 \times (G_{BP} - G_{RP})^2$, nor we did use G_{BP} information for the faint stars with $G_{BP} > 18$, which are affected by background underestimation (see Evans et al. 2018; Arenou et al. 2018). Moreover, we quadratically added 10 mmag to the uncertainties to take into account the systematics. We also took the 3 mmag mag^{-1} drift on the G band into account (Arenou et al. 2018; Weiler 2018). Concerning the *Gaia* astrometric information (Lindegren et al. 2018), we used the filter described in Eq. (1) of Arenou et al. (2018) to remove astrometry with large χ^2. We corrected the parallax zero point of −0.03 mas (Lindegren et al. 2018; Arenou et al. 2018) and removed obvious outliers having $\varpi + 3 \times \sigma_\varpi < 0$.

3. FEDReD in a nutshell

In this work, we used the FEDReD method that is presented in Babusiaux et al. (2020). Here we summarize the general FEDReD process we used to analyse a line of sight (LoS) and infer the relation between extinction and distance.

The algorithm works in two separate steps. The first deals with the individual analysis of each star contained in the LoS. It looks for $P\left(O_j \mid A_0, D\right)$, in other words, the likelihood of an observed star O_j (considering its apparent magnitudes and possibly its parallax) to be at a distance D with extinction A_0 (absorption at 550 nm). To compute this probability, FEDReD compares the apparent photometry of the star to an empirical Hertzprung-Russel diagram based on a *Gaia* DR2 representative of local thin disc stars. We took the colour- and extinction-dependant extinction coefficients into account by using Danielski et al. (2018) models with the same coefficients as those used in Lallement et al. (2019).

Once we computed the density of every star $P\left(O_j \mid A_0, D\right)$ in the LoS, we merged them to obtain an estimate of the joint distribution of extinction and distance of the entire field of view, $\hat{P}(A_0, D)$, using a Bayesian iterative Richardson-Lucy deconvolution (Richardson 1972; Lucy 1974). In other words, the prior of $P_k(A_0, D)$ of the kth iteration is the posterior of the $k-1$th iteration. To initiate the process, we built a simple prior $P_0(A_0, D)$ by multiplying two prior distributions: the distance distribution of stars, $P_0(d)$, and the distribution of extinction given the distance, $P_0(A_0 \mid D)$. The prior $P_0(D)$ simply follows a square law of the distance to take the cone effect into account. The prior $P_0(A_0 \mid D)$ is null where $A_0 > 10 \times D$ and flat elsewhere; this condition was experimentally verified using the map from Lallement et al. (2019); see Babusiaux et al. (2020) for more details.

Since we take the completeness into account, the result of the deconvolution is actually the estimate of the probability distribution $\hat{P}(A_0, D \mid S)$; here, S is the completeness of the LoS, which is the completeness of the 2MASS photometry. To model the completeness, we estimated the probability distribution of $P(S \mid A_0, D)$ using the empirical HR diagram and a rough completeness model. This distribution is used during the deconvolution process to obtain $\hat{P}(A_0, D \mid S)$, and the final $\hat{P}(A_0, D)$ distribution, that is derived from the process.

To obtain the relation $A_0(D)$ from the previous distribution, we used a Monte Carlo process to draw monotonic increasing relations in the distribution of $\hat{P}(A_0, D)$. We assessed the probability of each Monte Carlo solution (MCS) and we kept the 1000 best MCSs, which correspond to the 1000 best relations $A_0(D)$ of the LoS. Finally, we fitted a constrained median cubic spline through the MCS using `cobs` R library (Ng & Maechler 2007) to get the best fit for the given LoS.

We discretised the extinction-distance space that we probed. Here we chose a sampling from 0 to 30 mag with a step of 0.05 mag for the extinction. Concerning the distance space, it covers 0.1–30 kpc, but the step is linear in the distance modulus space with a width of 0.05 mag.

4. Merging line of sight results

To obtain an extinction map of the Galactic disc, we split it into small fields of view and analysed them separately with FEDReD. To ensure the continuity between LoSs, half of each LoS is shared with its two neighbouring fields. In practice this means that each star contributes to the information of two contiguous LoSs. This allows for an efficient post-processing. Indeed, the best fit output of FEDReD can be polluted by two major effects. On the one hand, the deconvolution can lead to very noisy $P(A_0, D)$, particularly in crowded fields where outliers can be numerous. On the other hand, several dust clumps could be present in the field of view and create an angular differential extinction that is difficult to handle with a single median spline fit. Thus we used the MCS information coming from neighbouring fields of view to remove outlier solutions and smooth the results.

To do so, we removed every MCS that is not included in the envelope drawn by the maximum and minimum values of the two neighbouring MCS envelopes. We repeated the operation until no more MCSs are removed; 30 to 60 iterations were usually needed to clean every LoS. This step converges thanks to the fact that two neighbour fields overlap, ensuring the consistency of two consecutive fields of view.

Once our sample was cleaned, we were able to draw a map by randomly picking one of the remaining MCSs for each LoS. We smoothed this map by averaging each field with its two direct neighbours, applying weights of 1/2, 1/4, and 1/4 for the centre field and the two sides, respectively, as each LoS is shared with its two neighbour fields. We drew 1000 of these smoothed maps. We then fitted a median constrained cubic spline on solutions using `cobs` to get the $A_0(D)$ relation of each LoS. To obtain the map of extinction density a_0, we decumulated the $A_0(D)$ relations by processing the difference between subsequent distance bins and normalised by the width of each distance bin.

Finally, we determined minimum and maximum valid distances for each field of view. This distance interval is defined by the observability of a red clump star in the infrared photometric band, considering the completeness of the field of view. We use red clump stars because their small intrinsic dispersion of absolute magnitude and colour leads to individual distributions

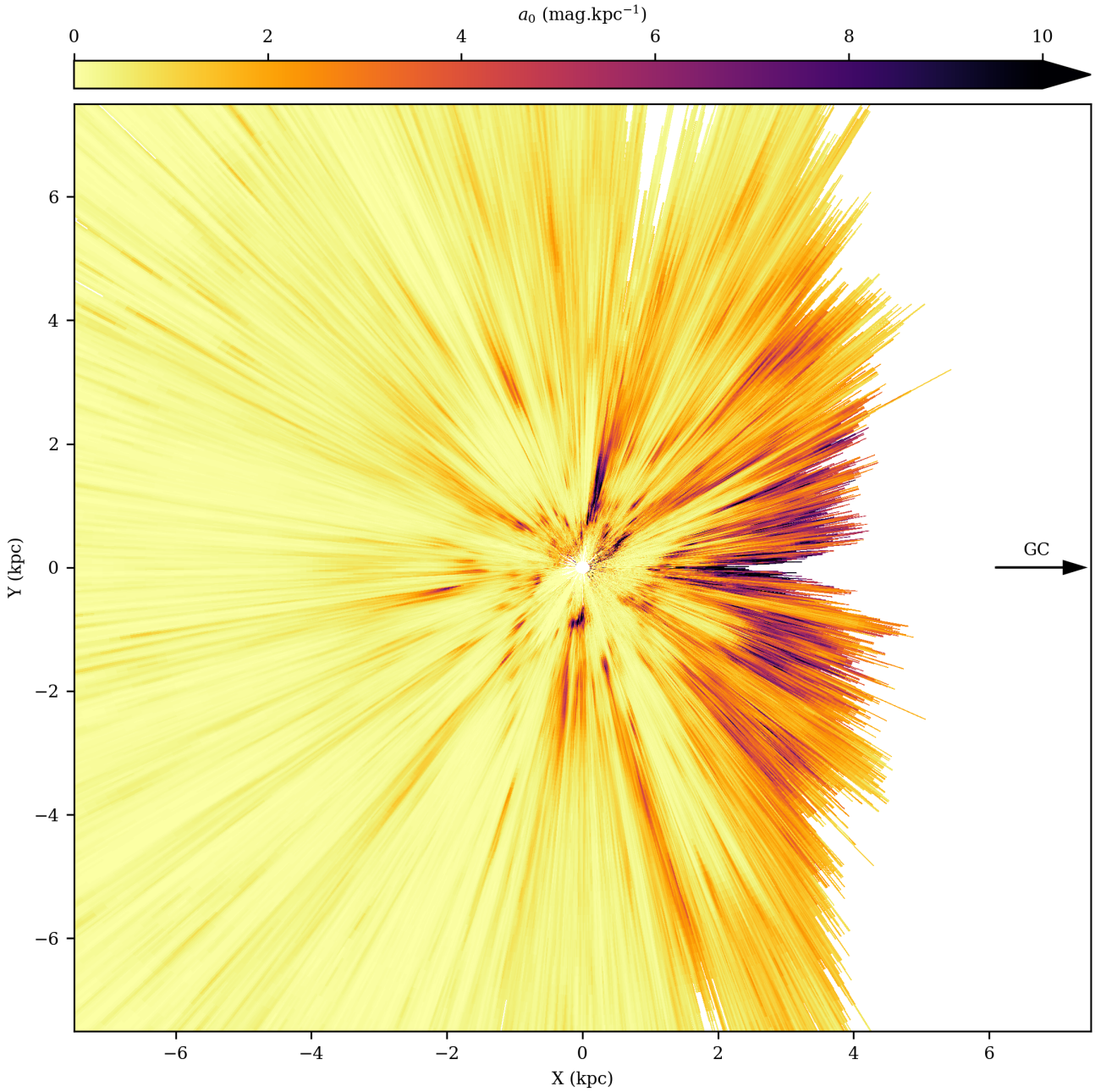

Fig. 1. Density of extinction a_0 at $b = 0°$. The Sun is at (0,0) and the Galactic centre direction is indicated by the black arrow.

$P\left(O_j \mid A_0, D\right)$ being more peaked than other stellar types, so they bring more constraints (Babusiaux et al. 2020). We processed the theoretical apparent magnitude of a red clump star by using the absolute magnitudes inferred by Ruiz-Dern et al. (2018) ($M_J = -0.95$ mag, $M_H = -1.45$ mag and $M_K = -1.61$ mag) and the best MCS for the $A_0(D)$ relation. Valid distances correspond to instances where the red clump's apparent magnitude is between the saturation and the completeness magnitudes of the field.

5. Results

The method described above was applied to 3 764 LoSs. Each LoS is centred at the Galactic latitude $b = 0°$ with a latitude width of 0.48°. The longitude width and position are defined so as to obtain fields of view that contain 3000 stars and share 1500 stars with each neighbour. This overlap with adjacent fields is necessary to properly clean MCSs by the neighbours minimum-maximum envelope. The average width of an LoS in the first and fourth quadrants is 0.12°, whereas the average width in the second and third quadrants is 0.43°. This difference is due to the larger number of observed stars in the central region of the Galaxy. The resulting extinction density map in the Galactic plane is presented in Fig. 1. The white area centred on the Sun corresponds to the too-close distances where the red clump is saturated (see previous section).

5.1. Uncertainty on the extinction and on the extinction density

By using the clean sample of MCSs, we were able to obtain the minimum and maximum cumulated extinction at each distance ($A_{0\min}(D)$ and $A_{0\max}(D)$).

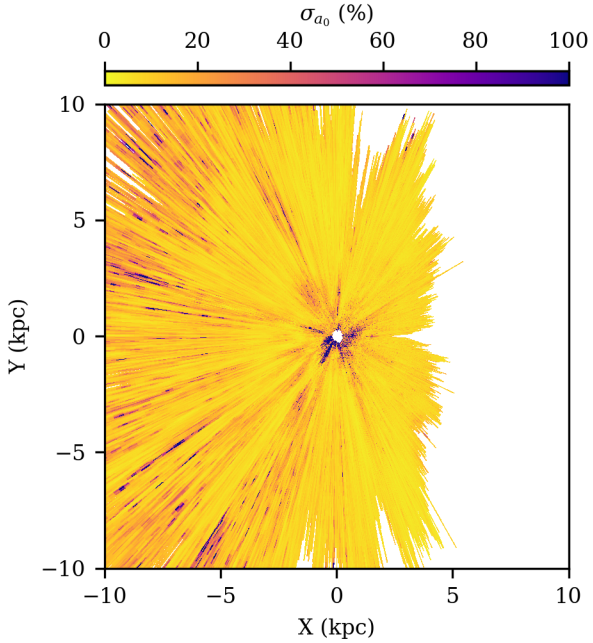

Fig. 2. Map of the relative error on extinction density, obtained by bootstraps.

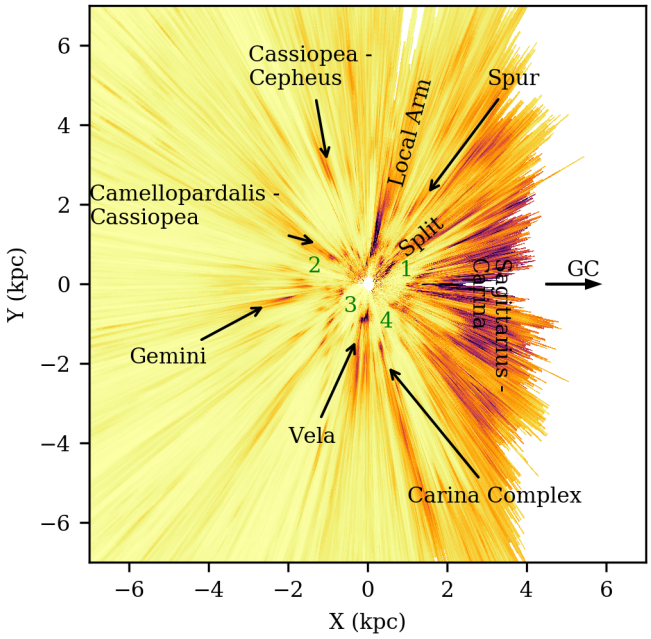

Fig. 3. Extinction map with labelled structures. The green numbers correspond to the four bubbles which delineate an empty region around the Sun with a butterfly shape (see text for description).

We also computed an error map of the extinction density. Basically, we applied a bootstrap technique to our sample of MCSs that had been cleaned of outliers. To do so, we kept a random subsample of MCSs for each LoS and applied the algorithm described above to obtain a bootstrapped map. We computed 100 of these bootstrapped maps and then processed the standard deviation at each (l, D) location to obtain the extinction density uncertainty. Figure 2 presents the relative uncertainty.

This error map mostly represents the sampling error, so it underestimates the true uncertainty of our results. The few locations where the relative uncertainty is very high either correspond to areas with almost no extinction or to areas with a high-increasing rate of extinction density (i.e. a high $\mathrm{d}a_0/\mathrm{d}D$), so the algorithm cannot precisely locate the beginning of the cloud. We also see that the uncertainty increases at large distances towards the anticentre.

5.2. Main structures

In Fig. 3 we label the main features visible on our map. We also overplot some other Inter-Stellar Medium (ISM) tracers on the map, in order to obtain a better view of the ISM structures. In Fig. 4 we add the molecular clouds of Miville-Deschênes et al. (2016). Figure 5 presents the HII region locations inferred by Hou & Han (2014), as well as the location of holes in the young star distribution found by Chen et al. (2019b). Finally, Fig. 6 represents masers from Reid et al. (2019).

The biggest structure on our map is the Sagittarius-Carinae complex, which extends in a cone between $\ell = 300°$ and $\ell = 30°$. Inside this high extinction area we notice a cavity centred on $\ell = 335°$, $D = 2$ kpc. This cavity presents an artefact which seems to be a Finger-of-God. This complex also contains a high density of molecular clouds and HII regions except in the cavity, which confirms the location and the size of this clean area.

Several high extinction structures related to spiral arms can be seen in the first quadrant. The local arm, at $\ell = 80°$, presents a very strong extinction consistent with the local arm masers of

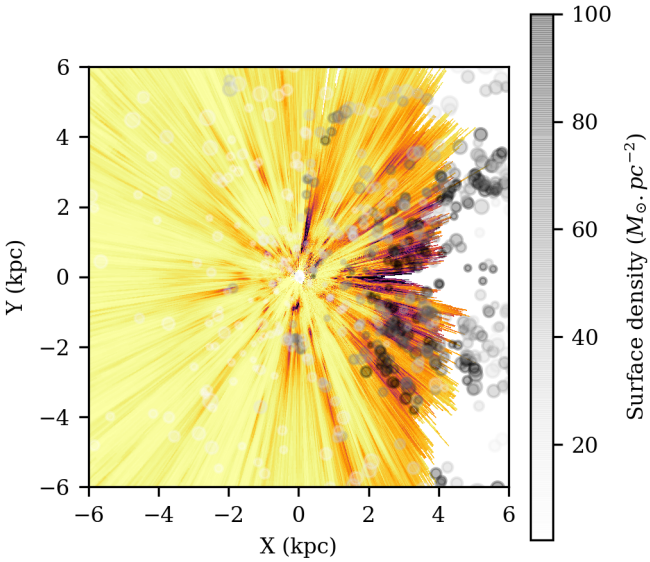

Fig. 4. Extinction map with Miville-Deschênes et al. (2016) CO clouds within $|b| < 0.24°$. Dot size is proportional to cloud size and the grey scale corresponds to the surface density.

Reid et al. (2019). The split (Lallement et al. 2019), between $\ell = 30°$ and $\ell = 40°$, is almost parallel to the local arm. We also notice the extinction overdensity at $\ell = 60°$ between $D = 1.5$ kpc and $D = 3.5$ kpc, which corresponds to the spur (Xu et al. 2018).

In the second quadrant, two main extinction overdensities appear. The first is at $\ell = 111°$ and $D = 3$ kpc and is associated with the Cassiopeia-Cepheus complex (Ungerechts et al. 2000). It coincides with the Reid et al. (2019) masers associated with the Perseus arm, and is also well-marked by HII regions. The second overdensity is the Cameliopardalis-Cassiopeia cloud (Chen et al. 2014) which is at $\ell = 145°$ and $1 \leq D \leq 3$ kpc.

The third quadrant contains many small high extinction areas associated with the local arm according to the masers or to the

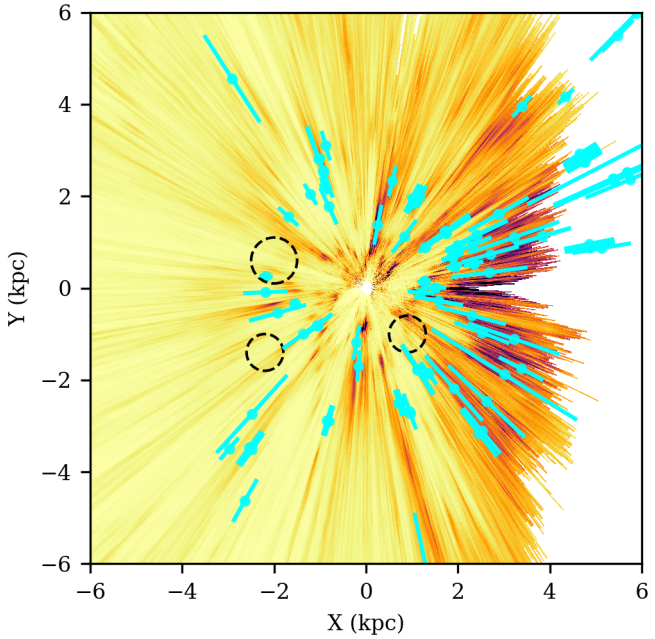

Fig. 5. Extinction map with the HII regions from Hou & Han (2014), keeping only regions with stellar distance information and with $|b| \leq 0.24°$. Circles correspond to holes in the young star distribution found by Chen et al. (2019b; Fig. 4).

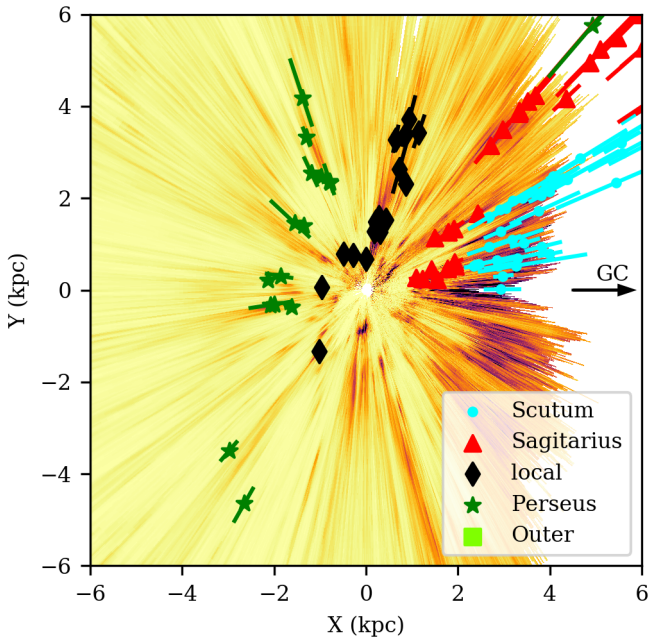

Fig. 6. Extinction map with masers from Reid et al. (2019). They are colour-coded by their spiral arm membership. We only plot masers with $|z| < 0.05$ kpc.

Radcliffe wave (Alves et al. 2020). There is also the Gemini molecular cloud (Carpenter et al. 1995) at ($\ell = 190°, D = 2$ kpc), which is related to masers of the Perseus arm.

The Vela cloud overlaps the third and the fourth quadrants. It exhibits a strong overdensity in the foreground and is prolonged by an empty bubble surrounded by a thin extinction edge. The distant boundary of this bubble is marked by molecular clouds and an HII region.

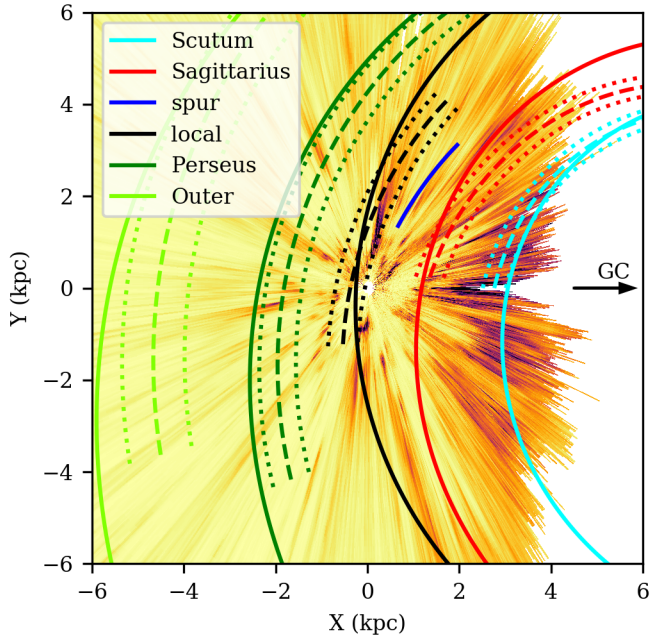

Fig. 7. Extinction map with the spiral arms from Reid et al. (2019) (dashed lines); from Hou & Han (2014) (solid lines); and the spur from Hou & Han (2014) (blue solid line) overplotted.

Near the Vela cloud, at $\ell = 282°$ and $D = 1.6$ kpc, the Carina complex (Zhang et al. 2001) also presents a strong foreground structure and is prolonged up to $D = 6$ kpc. This large elongation is also drawn by molecular clouds but the foreground structure only appears in extinction and is also clearly visible in Lallement et al. (2019).

In addition to all of these structures, the Sun appears surrounded by four bubbles without extinction, without taking the local bubble into account. The first is delimited by the Sagittarius-Carinae complex and the split. The second is centred on $\ell = 165°$. The third lies between the local arm masers and the Vela cloud. Finally, the longest one is surrounded by the Vela cloud and the Carina complex on one side, and by the Sagittarius-Carinae complex on the other side. These four extinction bubbles form a structure that we nickname "the Butterfly". These four bubbles also present a lack of every other ISM tracer. Chen et al. (2019b) also note holes in the distribution of young stars along the Perseus and Sagittarius arms, represented in Fig. 5. We notice in Chen et al. (2019b, Fig. 4) an underdensity of young stars in each bubble of the butterfly, with the exception of the third one.

5.3. Spiral structure

In Fig. 7 we overplot the spiral arms fitted by Reid et al. (2019) on masers, and the spiral arms fitted by Hou & Han (2014) on HII regions. While most of the masers and HII regions used to create these models have a footprint on the dust map (Figs. 6 and 5), the dust behaviour is very patchy and does not lead to obvious continuous spiral arm footprints.

The local arm is very well defined by the extinction in the first quadrant; however, its path in the third and fourth quadrants is not obvious. According to masers, it seems that the local arm does not really reach the Sun and misses the Vela complex to follow the Radcliffe wave (Alves et al. 2020). On the other hand, following the Hou & Han (2014) model, the Vela complex is part of the local arm.

The Sagittarius arm shows a strong extinction but it is cut into two parts by the first clean bubble. Moreover, it appears that the split of the local arm, even if it seems to be connected to the local arm at a close distance, is more related to the Sagittarius arm at a further distance. The spur looks like an extinction bridge between the local and the Sagittarius arms.

The Scutum arm crosses a high extinction area: however, we cannot distinguish a clear separation between the Scutum and the Sagittarius extinction areas. They are merged in the Sagittarius-Carina complex.

The Perseus arm is mostly visible at maser locations; it presents a very patchy structure (Baba et al. 2018) and is only noticeable thanks to the visual guide from Reid et al. (2014). Furthermore, the two masers of this arm at the bottom of the third quadrant are not even visible on our extinction map because their extinction signature is too small for our spatial resolution.

The outer arm is not visible on our extinction map. This is due to its high distance from the Galactic plane.

5.4. Comparison with other work

We compared our extinction map to one of the most complete available extinction maps of the solar neighbourhood, by Lallement et al. (2019). They essentially used the same data that we used in our study (2MASS and *Gaia*-DR2), but they restricted the analysis to stars with a relative parallax error better than 20%. Their results are presented in the reference extinction at 550 nm, as we do in this work. We present our map in Fig. 8, truncated to the same distance range as Lallement et al. (2019) and with the same colour map.

We note the very good agreement between the two maps within the confidence limit of the Lallement et al. (2019) results. The presence of Fingers-of-God on both maps is also apparent, though at different locations on the two maps, allowing us to positively identify them as spurious.

The foreground part of the Vela cloud is roughly identical in both works, which confirms this crescent shape. This particular morphology seems to appear as well in Fig. 12 of Chen et al. (2019a).

The split of the local arm, first described by Lallement et al. (2019), is also very strong in our result. Its closest part is roughly the same as on the Lallement et al. (2019) map. However, their method prevents them from detecting the elongation of the split as we do. This elongation is less sloping than the foreground part, in agreement with Chen et al. (2019a) and Green et al. (2019). The Cameliopardalis-Cassiopeia complex overdensity is at the same location in our work and in Lallement et al. (2019), Green et al. (2019), and Chen et al. (2019a).

However, we detect structures and prolongations of structures at larger distances, which did not appear in previous results in the literature. For example, the complete elongation of the Carina complex is too distant to be visible in Lallement et al. (2019) or in Chen et al. (2019a). Similarly, the split of the local arm is only visible locally in Lallement et al. (2019), which does not allow it to be linked with the Sagittarius-Carina complex. Chen et al. (2019a) and Green et al. (2019) do see a void between the split and Sagittarius, but at a location which actually contains masers.

6. Conclusion

We used data from about 5.6 million stars to produce an extinction map, reaching about 4 kpc in the direction of the Galactic

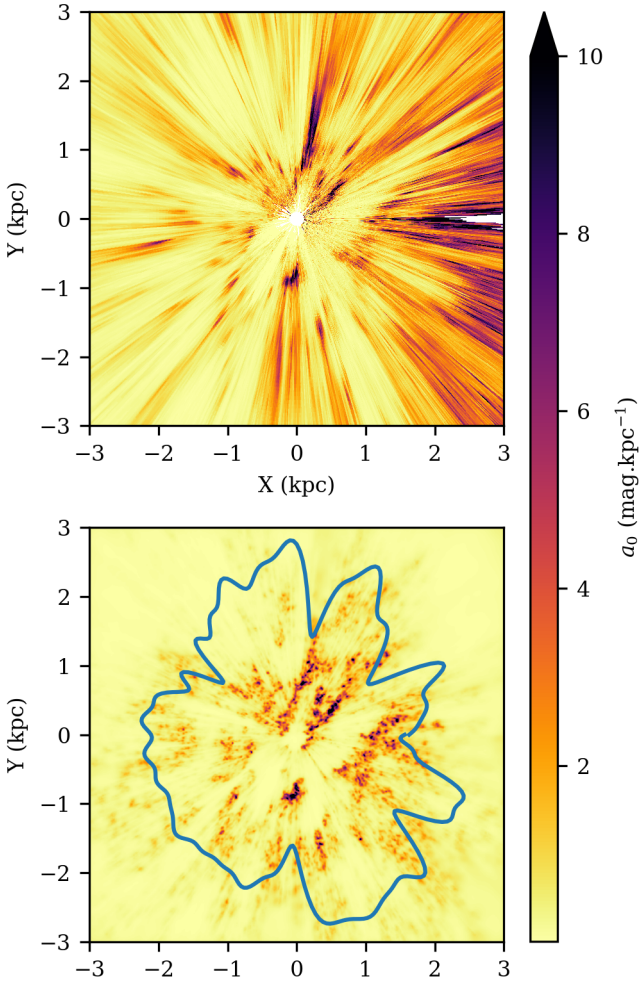

Fig. 8. Comparison with Lallement et al. (2019) results. Both maps are plotted with the same distance ranges and the same colour map. The blue curve represents the confidence limit of the Lallement et al. (2019) results.

Table 1. a_0 extinction density (in mag kpc^{-1}) of the map presented in Fig. 1.

	a_0 (mag kpc^{-1}) at different longitude				
D (kpc)	$\ell = 0.11°$	$\ell = 0.23°$	...	$\ell = 359.87°$	$\ell = 359.99°$
0.11					
...	...	...	...	...	
0.80	0.204	0.405	...		0.153
0.82	0.141	0.185	...	0.048	0.100
0.84	0.312	0.236	...	0.096	0.171
0.86	0.722	0.564	...	0.290	0.367
0.88	1.142	0.900	...	0.489	0.569
0.90	1.233	1.204	...	0.680	0.649
0.92	0.986	1.477	...	0.863	0.604
0.94	0.734	1.756	...	1.050	0.559
0.97	0.994	1.980	...	1.289	0.713
...	...	...	...	...	...

Notes. Each column corresponds to an LoS and the longitude is given in the first row (in degrees). The first column corresponds to the heliocentric distance in kiloparsecs. Blank spaces represent spatial locations outside of the distance confidence intervals (see Sect. 4). The full table is available in electronic form at the CDS.

Table 2. A_0 extinction (mag).

	A_0 (mag) at different longitude				
D (kpc)	$\ell = 0.11°$	$\ell = 0.23°$	...	$\ell = 359.87°$	$\ell = 359.99°$
0.11			...		
...	...	...	...	...	...
0.81	0.681	0.641	...	0.775	0.764
0.83	0.688	0.646	...	0.777	0.768
0.85	0.702	0.657	...	0.783	0.775
0.87	0.725	0.675	...	0.793	0.787
0.89	0.751	0.700	...	0.807	0.800
0.91	0.772	0.731	...	0.825	0.813
0.93	0.787	0.770	...	0.848	0.825
0.95	0.810	0.814	...	0.876	0.841
...	...	...	...	...	...

Notes. Each column corresponds to an LoS and the longitude is the first row (in degrees). The first column corresponds to the heliocentric distance in kiloparsecs. Blank spaces represent spatial locations outside of the distance confidence intervals (see Sect. 4). The full table is available in electronic form at the CDS.

Table 3. a_0 density uncertainty σ_{a_0} (in mag kpc^{-1}) presented in Fig. 2 (see Sect. 5.1).

	σ_{a_0} (mag kpc^{-1}) at different longitude				
D (kpc)	$\ell = 0.11°$	$\ell = 0.23°$	...	$\ell = 359.87°$	$\ell = 359.99°$
0.11			...		
...	...	...	...	...	...
0.80	0.111	0.109	...		0.055
0.82	0.137	0.092	...	0.062	0.065
0.84	0.145	0.104	...	0.067	0.086
0.86	0.160	0.100	...	0.077	0.101
0.88	0.199	0.077	...	0.062	0.108
0.90	0.232	0.085	...	0.060	0.115
0.92	0.221	0.079	...	0.090	0.128
0.94	0.209	0.082	...	0.115	0.147
0.97	0.307	0.108	...	0.150	0.170
...	...	...	...	...	...

Notes. Each column corresponds to an LoS and the longitude is the first row (in degrees). The first column corresponds to the heliocentric distance in kiloparsecs. Blank spaces represent spatial locations outside of the distance confidence intervals. The full table is available in electronic form at the CDS.

Table 4. Maximum values of the extinction A_0 (see Sect. 5.1).

	$A_{0\max}$ (mag) at different longitude				
D (kpc)	$\ell = 0.11°$	$\ell = 0.23°$	...	$\ell = 359.87°$	$\ell = 359.99°$
0.11			...		
...	...	...	...	...	...
0.81	0.750	0.850	...	0.900	0.900
0.83	0.750	0.850	...	0.900	0.900
0.85	0.900	0.850	...	0.900	1.000
0.87	0.900	0.850	...	0.900	1.000
0.89	0.900	0.850	...	0.900	1.000
0.91	0.900	0.850	...	0.900	1.000
0.93	0.900	0.850	...	0.900	1.000
0.95	1.000	1.000	...	0.900	1.000
...	...	...	...	...	...

Notes. Each column corresponds to an LoS and the longitude is the first row (in degrees). The first column corresponds to the heliocentric distance in kiloparsecs. Blank spaces represent spatial locations outside of the distance confidence intervals. The full table is available in electronic form at the CDS.

Table 5. Minimum values of extinction A_0 (see Sect. 5.1).

	$A_{0\min}$ (mag) at different longitude				
D (kpc)	$\ell = 0.11°$	$\ell = 0.23°$	...	$\ell = 359.87°$	$\ell = 359.99°$
0.11			...		
...	...	...	...	...	...
0.81	0.550	0.550	...	0.600	0.600
0.83	0.600	0.550	...	0.600	0.600
0.85	0.600	0.550	...	0.600	0.600
0.87	0.600	0.550	...	0.600	0.600
0.89	0.600	0.600	...	0.600	0.600
0.91	0.600	0.600	...	0.650	0.700
0.93	0.600	0.700	...	0.650	0.700
0.95	0.650	0.750	...	0.650	0.700
...	...	...	...	...	...

Notes. Each column corresponds to an LoS and the longitude is the first row (in degrees). The first column corresponds to the heliocentric distance in kiloparsecs. Blank spaces represent spatial locations outside of the distance confidence intervals. The full table is available in electronic form at the CDS.

centre and more than 6 kpc in other directions. Thanks to this result, we are able to confirm general structures of the solar neighbourhood that had already been revealed by recent works (Lallement et al. 2019; Green et al. 2019; Chen et al. 2019a). The local arm and the split represent two structures that are close to the Sun and have a high extinction separated by a clean corridor. Nevertheless, our map reveals a possible relation between the split and the Sagittarius arm at a larger distance. The Galactic centre direction is dominated by the Sagittarius-Carina complex. Because of this high extinction, as well as crowding, we are not able to go beyond this complex. We do not distinguish the Sagittarius and the Scutum arm within this complex. The Perseus arm extinction component seems very fragmented, even if the location of the masers that trace this arm are visible in the dust. The Vela and Carina complexes are the two strongest extinction areas in the forth quadrant. Furthermore, FEDReD's map reveals the extinction prolongation of the Carina complex and the bubble structure behind the Vela cloud. Finally, we also observe four empty bubbles close to the Sun, and we reveal the ends of two of them.

Data corresponding to the maps presented here are available in Tables 1 and 3. We also provide the values of the cumulated extinction A_0 and corresponding asymmetric uncertainties in Tables 2, 4, and 5. The full versions are available in machine-readable form at the CDS.

In future works, we will also explore the Galactic disc at higher and lower latitudes. This will allow for a better study of some structures, for example the Outer arm which is known to be warped.

To explore larger distances, and in particular the Galactic centre and the start of the spiral arms, we will use deeper near-infrared surveys, such as UKIDSS (Lucas et al. 2008) and VISTA

(Minniti et al. 2010). Moreover, we look forward to the third data release of the *Gaia* mission, which will provide better parallax and photometry constraints.

Acknowledgements. We thank the referee for suggestions that improved the paper. This work has made use of data from the European Space Agency (ESA) mission *Gaia* (https://www.cosmos.esa.int/gaia), processed by the *Gaia* Data Processing and Analysis Consortium (DPAC, https://www.cosmos.esa.int/web/gaia/dpac/consortium). Funding for the DPAC has been provided by national institutions, in particular the institutions participating in the *Gaia* Multilateral Agreement. This publication also makes use of data products from the Two Micron All Sky Survey, which is a joint project of the University of Massachusetts and the Infrared Processing and Analysis Center/California Institute of Technology, funded by the National Aeronautics and Space Administration and the National Science Foundation. We benefitted from the computing resources of MesoPSL financed by the Region Ile de France and the project Equip@Meso (reference ANR-10-EQPX-29-01).

References

Alves, J., Zucker, C., Goodman, A. A., et al. 2020, Nature, 578, 237
Arenou, F., Grenon, M., & Gomez, A. 1992, A&A, 258, 104
Arenou, F., Luri, X., Babusiaux, C., et al. 2018, A&A, 616, A17
Baba, J., Kawata, D., Matsunaga, N., Grand, R. J. J., & Hunt, J. A. S. 2018, ApJ, 853, L23
Babusiaux, C., Fourtune-Ravard, C., Hottier, C., Arenou, F., & Gomez, A. 2020, A&A, 641, A78
Capitanio, L., Lallement, R., Vergely, J. L., Elyajouri, M., & Monreal-Ibero, A. 2017, A&A, 606, A65
Carpenter, J. M., Snell, R. L., & Schloerb, F. P. 1995, ApJ, 445, 246
Chen, B. Q., Schultheis, M., Jiang, B. W., et al. 2013, A&A, 550, A42
Chen, B.-Q., Liu, X.-W., Yuan, H.-B., et al. 2014, MNRAS, 443, 1192
Chen, B.-Q., Huang, Y., Yuan, H.-B., et al. 2019a, MNRAS, 483, 4277
Chen, B.-Q., Huang, Y., Hou, L.-G., et al. 2019b, MNRAS, 487, 1400
Danielski, C., Babusiaux, C., Ruiz-Dern, L., Sartoretti, P., & Arenou, F. 2018, A&A, 614, A19
Evans, D. W., Riello, M., Angeli, F. D., et al. 2018, A&A, 616, A4
Fitzgerald, M. P. 1968, AJ, 73, 983
Gaia Collaboration (Brown, A. G. A., et al.) 2018, A&A, 616, A1
Green, G. M., Schlafly, E. F., Finkbeiner, D. P., et al. 2014, ApJ, 783, 114
Green, G. M., Schlafly, E. F., Finkbeiner, D. P., et al. 2015, ApJ, 810, 25
Green, G. M., Schlafly, E. F., Finkbeiner, D., et al. 2018, MNRAS, 478, 651
Green, G. M., Schlafly, E., Zucker, C., Speagle, J. S., & Finkbeiner, D. 2019, ApJ, 887, 93
Hakkila, J., Myers, J. M., Stidham, B. J., & Hartmann, D. H. 1997, AJ, 114, 2043
Hou, L. G., & Han, J. L. 2014, A&A, 569, A125
Lallement, R., Babusiaux, C., Vergely, J. L., et al. 2019, A&A, 625, A135
Lindegren, L., Hernández, J., Bombrun, A., et al. 2018, A&A, 616, A2
Lucas, P. W., Hoare, M. G., Longmore, A., et al. 2008, MNRAS, 391, 136
Lucy, L. B. 1974, AJ, 79, 745
Marrese, P. M., Marinoni, S., Fabrizio, M., & Altavilla, G. 2019, A&A, 621, A144
Marshall, D. J., Robin, A. C., Reylé, C., Schultheis, M., & Picaud, S. 2006, A&A, 453, 635
Minniti, D., Lucas, P., Emerson, J., et al. 2010, New Astron., 15, 433
Miville-Deschênes, M.-A., Murray, N., & Lee, E. J. 2016, ApJ, 834, 57
Neckel, T., & Klare, G. 1980, A&AS, 42, 251
Ng, P., & Maechler, M. 2007, Stat. Modell. Int. J., 7, 315
Reid, M. J., Menten, K. M., Brunthaler, A., et al. 2014, ApJ, 783, 130
Reid, M. J., Menten, K. M., Brunthaler, A., et al. 2019, ApJ, 885, 131
Rezaei Kh., S., Bailer-Jones, C. A. L., Hogg, D. W., & Schultheis, M. 2018, A&A, 618, A168
Richardson, W. H. 1972, J. Opt. Soc. Am., 62, 55
Robin, A. C., Luri, X., Reylé, C., et al. 2012, A&A, 543, A100
Ruiz-Dern, L., Babusiaux, C., Arenou, F., Turon, C., & Lallement, R. 2018, A&A, 609, A116
Sale, S. E., Drew, J. E., Barentsen, G., et al. 2014, MNRAS, 443, 2907
Schultheis, M., Chen, B. Q., Jiang, B. W., et al. 2014, A&A, 566, A120
Skrutskie, M. F., Cutri, R. M., Stiening, R., et al. 2006, AJ, 131, 1163
Ungerechts, H., Umbanhowar, P., & Thaddeus, P. 2000, ApJ, 537, 221
Vergely, J.-L., Freire Ferrero, R., Siebert, A., & Valette, B. 2001, A&A, 366, 1016
Weiler, M. 2018, A&A, 617, A138
Xu, Y., Bian, S. B., Reid, M. J., et al. 2018, A&A, 616, L15
Zhang, X., Lee, Y., Bolatto, A., & Stark, A. A. 2001, ApJ, 553, 274